





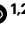






Vertical iontronic energy storage based on osmotic effects and electrode redox reactions

Received: 18 January 2023

Accepted: 1 December 2023

Published online: 5 January 2024

 Check for updates

Feiyao Yang ¹, Puguang Peng ^{1,2}, Zhao-Yi Yan ³, Hongzhao Fan⁴, Xiang Li ^{1,2}, Shaoxin Li ^{1,2}, Houfang Liu³, Tian-Ling Ren ³, Yanguang Zhou ⁴, Zhong Lin Wang ^{1,2,5}  & Di Wei ¹ 

Making salinity gradient energy practical is a great challenge. Despite recent advancements, the practicality of osmotic energy for portable electronics remains doubtful due to its limited power output and portability constraints. Here we report a method for optimizing the transport of alkali metal ions within two-dimensional nanofluidic channels and coupling it with tailored interfacial redox reactions to store the osmotic energy in a space of tens of micrometres within the cut edge of a polymer film. An ultrahigh output power density of $15,900 \text{ W m}^{-2}$ has been achieved. By connecting the devices in series, commercial electronics can be powered due to the high volumetric specific energy density (9.46 Wh cm^{-3}) and power density (106.33 W cm^{-3}). This work introduces an approach for storing iontronic energy based on osmotic effects, providing a platform for developing renewable, ultrathin and safe power sources.

Ion channels in cellular membranes are crucial for life's essential functions¹. Ultrafast ion transport within nano/subnano-sized ion channels has enabled the generation of biological energy, such as in adenosine triphosphate synthesis for the origin of life². To mimic and understand the function of such ion-transport systems, it is desirable to investigate artificial nanometric channels with similar dimensions. Ions can be transported within two-dimensional (2D) nanofluidic channels in a highly efficient way due to the nanoconfinement effect, enabling bionic iontronics³. Iontronics offers the possibility of controlling the ionic flux, leading to applications in actuators⁴, sensors⁵ and memristors³ and a better understanding of the charging dynamics in batteries and supercapacitors⁶. Graphene oxide (GO), as a typical 2D nanofluidic material, has been reported to provide a nanoconfined charging dynamic medium with potential use in many applications such as ionic analogue and voltage gating devices⁷. Although the GO flake size can be polydisperse, the restacked structure can still readily produce numerous

interconnected 2D nanofluidic channels in printed/drop-cast GO-based iontronics. Properly constructed GO 2D nanofluidic structures possess abundant interconnected horizontal channels with a negative surface charge for fast cation transport⁸, and higher-than-bulk ionic conductivity has been observed⁹. Given these advantageous features, together with the natural void space provided by the nanofluidic channels that can buffer volume changes during charge–discharge cycles¹⁰, the nanofluidic structure could offer an excellent electrochemical performance as a medium for ion transport and storage in energy devices. For this reason, nanofluidic materials with tailored ion-transport dynamics have recently been explored to efficiently harvest renewable osmotic energy^{11,12}.

Osmotic energy originates from a salinity gradient, leading to the release of Gibbs free energy that can be harvested and converted into electrical energy. Reverse electrodialysis (RED) is one of the most common methods used for osmotic energy conversion¹³, and

¹Beijing Institute of Nanoenergy and Nanosystems, Chinese Academy of Sciences, Beijing, People's Republic of China. ²School of Nanoscience and Engineering, University of Chinese Academy of Sciences, Beijing, People's Republic of China. ³Beijing National Research Center for Information Science and Technology, School of Integrated Circuits, Tsinghua University, Beijing, People's Republic of China. ⁴Department of Mechanical and Aerospace Engineering, The Hong Kong University of Science and Technology, Hong Kong, People's Republic of China. ⁵Yonsei Frontier Lab, Yonsei University, Seoul, Republic of Korea.  e-mail: zhong.wang@mse.gatech.edu; weidi@binn.cas.cn

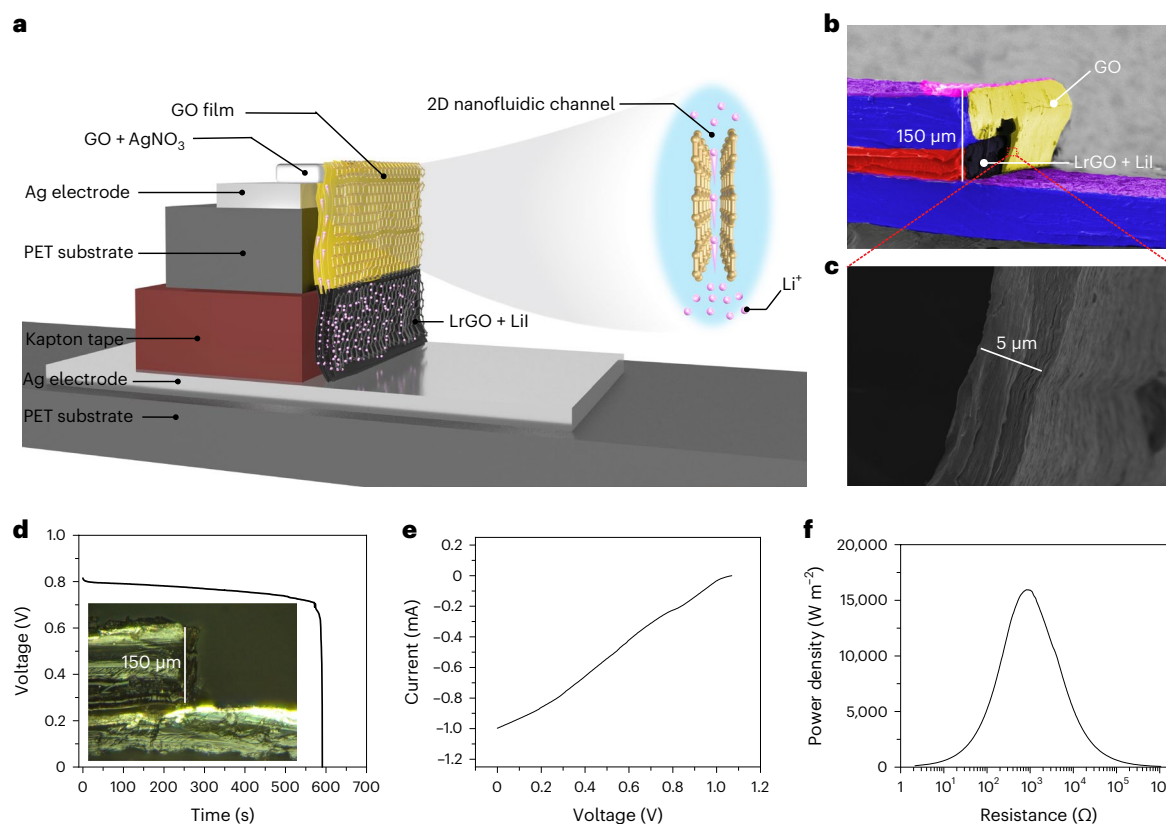


Fig. 1 The vertical iontronic energy storage device. **a**, Schematic illustration of the vertical structure and mechanism of lithium-ion (Li⁺) transport within the 2D nanofluidic channels. **b**, False-coloured SEM image of the device (cross section) showing the GO film layer (yellow), the LrGO + Lil layer (black), the PET layer (blue), the Ag electrode layer (purple), the Kapton tape layer (red) and the GO + AgNO₃ layer (pink). **c**, SEM image of the GO film layer (cross section).

d, Galvanostatic discharge performance of the device at 100 μA (25 °C, 80% RH). Inset: an optical image of the device (cross section). **e**, Current–voltage characteristics of the device at a scan rate of 10 mV s⁻¹ (25 °C, 80% RH). **f**, Output power density as a function of the electronic load resistance. The output power density reaches a peak value of 15,900 W m⁻² at a load resistance of ~835 Ω.

investigations have focused on ion-selective membranes to increase the ion transport and lower the internal resistance¹². The limitations of ion-selective membranes, such as their high membrane resistance and low mass-transport efficiency, result in a power density (<2.2 W m⁻²) that is economically unviable¹². Although the conversion of osmotic energy has been reported to be boosted by a three-dimensional hydrogel interface¹⁴, the power density of most osmotic power sources is generally small, ranging from 0.35 W m⁻² to around 5 W m⁻² in previous reports^{14–17}. There is a competitive relationship between the selectivity and permeability of the ion-selective membrane, and the ideal optimized thickness is supposed to be less than 1 μm (ref. 18), which is difficult to obtain. An ultrathin interfacial synthetic membrane was developed to enable a considerable power density (~67 W m⁻²)¹⁹, but the scalability was limited by the low mechanical strength¹². Theoretically, an estimated power density of 10⁶ W m⁻² could be reached if a single-layer MoS₂ membrane with a homogeneous pore size of 10 nm and a porosity of 30% could be exploited²⁰. In practice, using single conical pore of 400 nm on polyethylene terephthalate (PET) or through a boron–nitride nanotube, power density values of 945 W m⁻² and 4,000 W m⁻², respectively, have been achieved^{11,21}. However, these reported examples of osmotic power generation with ultrahigh power density were all based on single nanopores and operated at the nanoampere or picowatt level²¹. In addition, the power density would decrease significantly in going from the single- to multi-pore level (to the range of only a few watts per square metre)¹² because of the strong pore–pore interactions and an increase in the ion concentration polarization^{12,22}. Although ion-selective membranes have always been a key factor in RED-based osmotic energy conversion¹², the choice of a

suitable electrode system is also critical¹³. Optimized electrode materials and redox couples will improve the total power of the osmotic power source^{23–25}. Moreover, in a report with the maximum theoretical osmotic power density of 10⁶ W m⁻², it was mentioned that substantial power generation and considerable energy can be achieved using a tailored chemical potential difference for its practicality²⁰.

In this work, inspired by both the efficient ion-transport dynamics within the 2D nanofluidic channels of GO and tailored interfacial redox reactions, we developed a solid-state iontronic energy storage device powered purely by the humidity of ambient air. Various GO-based inks were sprayed onto the charge collectors using an ultrasonic spray-coating system and then dried on the PET substrate to fabricate the device. As the GO ink dried, the 2D nanofluidic channels of GO were formed. The electrode gap of the device, covered by GO, is equal to the thickness of the ion-selective membrane in a conventional osmotic power source. We devised a vertical strategy using the edge of a PET substrate and Kapton film (Fig. 1a–c), which offered the capability to scale down the ion-transport distance (equivalent to a decrease in the thickness of the ion-selective membrane). The transport rate of alkali metal ions within the GO nanofluidic channels was studied through experiments and simulations to select the fastest cation, thereby reducing the internal resistance. Furthermore, tailored interfacial redox reactions on the electrode surface were introduced to enhance the power, enabling the device to be discharged at 100 μA (Fig. 1d), and with its short-circuit current (*I*_{sc}) surging to almost 1 mA (Fig. 1e). A maximum output power density of 15,900 W m⁻² was obtained via the combination of efficient cation transport and tailored redox reactions (Fig. 1f, Supplementary Table 1 and Supplementary Note 1).

Working mechanism of the iontronic device

To reveal the mechanism of the iontronic energy storage device, gold (Au) was used as the charge collector to exclude possible electrochemical reactions from the electrode itself. GO, with abundant oxygen-containing functional groups, forms 2D nanofluidic channels with a negative surface charge (Supplementary Fig. 1)^{26,27}. Potassium hydroxide (KOH) was added to the GO solution to partially remove the oxygen-containing functional groups^{28,29}, and when KOH was added the colour of the GO solution changed from light yellow to dark brown. In our previous work³⁰, such a KOH-treated GO solution was referred to as a reduced graphene oxide (rGO) ink. As an ideal reducing reagent for GO, L-ascorbic acid (LAA) was also used to reduce the GO to obtain LAA-reduced GO (LrGO) ink. The zeta potential of the three GO-based inks (GO, rGO and LrGO) was measured to be -59.5 , -56.9 and -21.9 mV, respectively (Supplementary Fig. 1a), which confirmed the removal of some of the negatively charged oxygen-containing functional groups from pristine GO. This was consistent with the Fourier transform infrared spectra of the ink samples (Supplementary Fig. 1b). Although trace amounts of potassium remain from the GO manufacturing process (Supplementary Fig. 2a,b), the cation concentration is much lower than that in rGO, which contains a relatively large amount of potassium (Supplementary Fig. 2c,d). To study the disorder and defects of GO and rGO, Raman spectroscopy was performed (Supplementary Fig. 3). The D and G peaks were, respectively, close to $1,350\text{ cm}^{-1}$ and $1,580\text{ cm}^{-1}$, consistent with previously reported results²⁹. Compared with the D band to G band intensity ratio (I_D/I_G) of GO (0.98), I_D/I_G for rGO (1.15) was higher. The increase in I_D/I_G indicated an increase in defects, which may be due to a reduction in the flake size from the reaction of KOH with the functional groups of the GO layer. Furthermore, from particle size analysis the flake size of rGO ($D_{90} = 58.72\text{ }\mu\text{m}$) was indeed confirmed to be smaller than that of GO ($D_{90} = 70\text{ }\mu\text{m}$; Supplementary Fig. 4a,b), indicating the GO flakes may be partially destroyed by KOH. The further decrease in flake size of LrGO ($D_{90} = 53.95\text{ }\mu\text{m}$) indicated more intense reactions between LAA and GO during the chemical reduction process (Supplementary Fig. 4c).

The Au electrodes were prepared by evaporating Au onto the PET substrate through a shadow mask. The size of the Au electrode pad was $5 \times 5\text{ mm}$, and the gap between the Au electrodes was 2 mm . GO ink was sprayed and dried on one of the Au electrodes using an ultrasonic spray-coating system, and then rGO ink was sprayed and dried on the other electrode to form a junction with the GO (Supplementary Fig. 5a). The scanning electron microscope (SEM) image (Fig. 1c) showed that the cross-section structure of the GO film was similar to that in previous reports^{25,31}, which indicated that the 2D nanofluidic channels had been constructed. Potassium ions (K^+) migrated rapidly from the rGO side to the GO side through the GO/rGO junction in the ambient-humidity environment³⁰. From the Raman spectrum (Supplementary Fig. 5b), I_D/I_G of GO after discharge was 1.05, which is higher than that of pristine GO (0.98). This may be due to the migration of K^+ from rGO to the GO side, and the insertion of K^+ within the GO layers brought more defects. After discharge, the interlayer spacing of the GO flakes increased from 7.7 \AA to 8.9 \AA , as confirmed from the X-ray diffraction patterns (Supplementary Fig. 5c). Moreover, results from inductively coupled plasma optical emission spectrometry (ICP-OES) indicated that the concentration of elemental potassium in the GO increased from $1,755\text{ ppm}$ to $37,357\text{ ppm}$ after discharge. This provided direct evidence of K^+ transportation from rGO to GO (Supplementary Fig. 5d).

A series of rGO inks with different K^+ concentrations was prepared to study the influence of different ion gradients on the iontronic energy storage device (Supplementary Fig. 6). The device (Au/GO/rGO/Au) generated a high voltage of 0.93 V in an atmosphere that had a relative humidity (RH) of 80% at $25\text{ }^\circ\text{C}$, although the I_{sc} was very small (Supplementary Fig. 7a). The directional migration of ions from high concentration to low concentration can be converted to electron transportation at the surface of the electrodes via redox reactions in RED systems¹³.

In our case, as an inert metal, Au itself does not participate in the electrochemical reactions. However, there may be some redox reactions occurring on the surface of the Au electrodes, and a combination of the diffusion potential (E_{diff}) and the redox potential (E_{redox}) resulted in an open-circuit voltage (V_{oc}) of 0.93 V for the device (Au/GO/rGO/Au). Since the solid-state device was working in an open environment, the moisture or oxygen in the air may participate in the redox reactions, which was verified using cyclic voltammetry (Supplementary Fig. 7b). As discussed in Supplementary Note 2, the measured voltage (V_{oc}) of the device (Au/GO/rGO/Au) consisted of $E_{\text{redox}} = 0.59\text{ V}$ and $E_{\text{diff}} = 0.34\text{ V}$ (Supplementary Table 2). Because of the weak and unstable redox reaction, the discharge curves showed a correspondingly low energy capacity (Supplementary Fig. 7c).

Room-temperature ionic liquids (RTILs) have been reported to enhance the I_{sc} of iontronics³². Compared with organic electrolytes, RTILs have stable physical and chemical properties, such as low volatility, a wide electrochemical window, non-flammability, high thermal stability and so on³³, which will guarantee the reliability of the device without evaporation of the electrolyte. Because of its relatively high ionic conductivity (7.1 mS cm^{-1}) and low melting point ($-35.5\text{ }^\circ\text{C}$)³⁴, the triethylsulfonium bis(trifluoromethylsulfonyl)imide ([TES][TFSI]) RTIL was used to boost the current of the iontronic energy storage device. As shown in Supplementary Fig. 7a, the I_{sc} of the Au/GO/RTIL/rGO/Au device was higher than that of the Au/GO/rGO/Au device, but the V_{oc} of Au/GO/RTIL/rGO/Au was the same as that of Au/GO/rGO/Au. The role of the RTIL may be chiefly to enhance the current of the device (Supplementary Fig. 7c).

Iontronic device with tailored interfacial redox reactions

RED based on electrode redox reactions is an efficient method for directly extracting electrical energy from salinity gradients, and the choice of a suitable electrode system is a key factor¹³. To improve the performance of the RED-based osmotic power source, redox reactions on the cathode and anode surfaces of a device with Ag electrodes were designed. A pair of Ag electrodes was printed on the PET substrate via screen printing. In succession, GO/AgNO₃ and GO inks were sprayed onto and dried on one of the Ag electrode pads to form the cathode side using an ultrasonic spray-coating system, and then the anode side of the Ag electrode was covered with the LrGO-containing alkali iodide salt (AIS) in the same way, overlapping with the GO film to form the junction of the planar device (Fig. 2a). Compared with chlorine and bromine, the standard electrode potential of iodine versus the NHE (normal hydrogen electrode) was the lowest for the formation of the silver halide³⁵, resulting in the highest E_{redox} among the halogen sequences (Supplementary Note 3 and Supplementary Fig. 8). Different AISs (for example, potassium iodide (KI), sodium iodide (NaI) and lithium iodide (LiI)) of the same concentration were added to the anode side to introduce an oxidation reaction with the printed Ag electrode. For such planar devices with AISs, the ion gradient of alkali metal cations between the cathode and the anode generated the osmotic energy, while silver ions (Ag^+) in the silver nitrate (AgNO_3) were reduced at the cathode side ($\text{Ag}^+ + \text{e}^- \rightleftharpoons \text{Ag}$) and the Ag electrode was oxidized to form silver iodide (AgI) at the anode side ($\text{Ag} + \text{I}^- \rightleftharpoons \text{AgI} + \text{e}^-$). As shown in Fig. 2b, the V_{oc} values for the planar devices with an AIS were all -1.05 V , but the I_{sc} of the device with LiI was higher compared with the other AIS counterparts (KI and NaI). This may be because the device with LiI possesses a lower internal resistance and a correspondingly higher ionic conductivity. Nyquist plots from the electrochemical impedance spectra (Supplementary Fig. 9) were compared and fitted via the most commonly used equivalent circuit for porous electrodes (inset of Supplementary Fig. 9). The device with LiI possessed not only the smallest equivalent series resistance (R_s) but also the smallest charge-transfer resistance (R_{ct}) among all of the AIS-containing devices, as shown in Supplementary Table 3. These results were also consistent with the

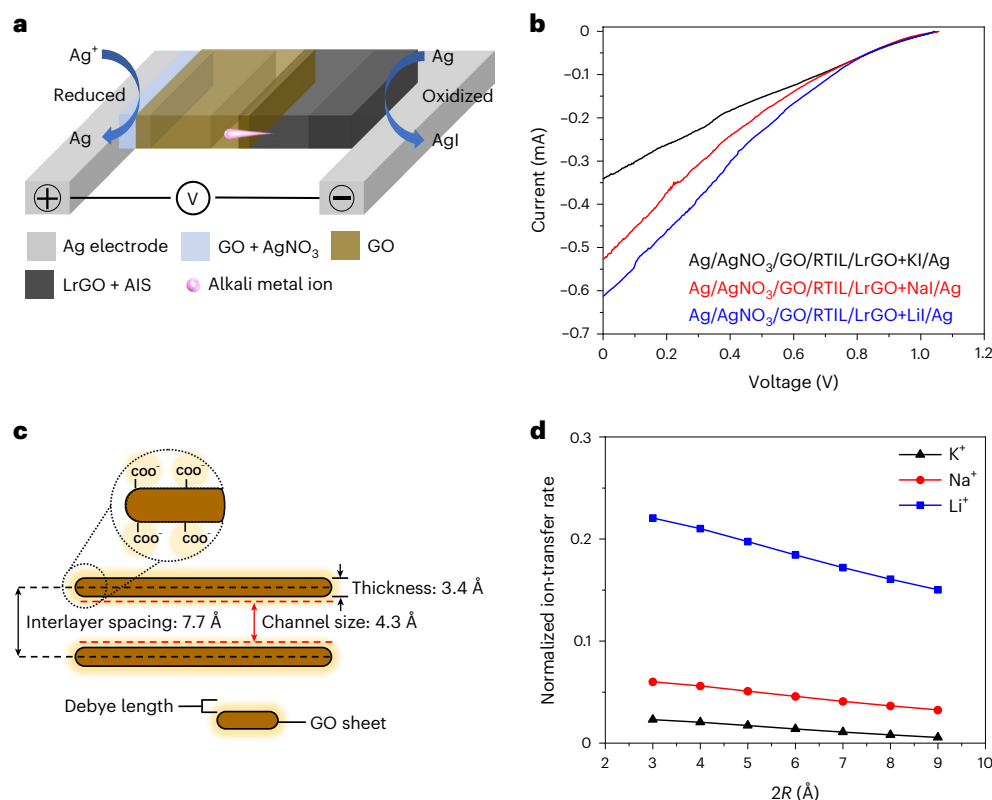


Fig. 2 | Characterization of ion-transport properties in the planar iontronic energy storage devices with an AIS. **a**, Structure of the device with the AIS. **b**, Current–voltage characteristics of the devices with different AISs (KI, NaI and LiI) at a scan rate of 10 mV s⁻¹ (25 °C, 80% RH). **c**, Schematic of the GO nanofluidic

channel and its size. **d**, Transport properties of the dehydrated bare alkali metal ions simulated in a subnanopore under the experimental conditions (surface charge density = 0.06 C m⁻², effective osmotic voltage = 0.4 V, RH = 80%, length of the channel = 5 Å).

ionic conductivity values measured from the physically confined GO film (Supplementary Discussion, Supplementary Notes 4–7, Supplementary Tables 4–6 and Supplementary Figs. 10–14), which revealed that the ionic conductivity of the alkali metal ions in the GO nanofluidic channels may be correlated with the ion type (Supplementary Fig. 12 and Supplementary Table 4)³⁶. As shown in Supplementary Fig. 5c, the interlayer spacing of pristine GO was 7.7 Å. By subtracting the thickness of the GO layer (3.4 Å), the effective channel size was about 4.3 Å (Fig. 2c), which was smaller than the typical size of the hydration shell of the ions (1–2 nm)³⁷. The alkali metal ions inside the GO film were likely to be partially hydrated once driven by the humidity in ambient air. As described in Supplementary Note 8, we systematically measured the ion-transport rates of the alkali metal ions (Li⁺, Na⁺ and K⁺) using ICP-OES and found evidence for the different selectivity of the alkali metal ions within the 2D nanofluidic channels (Supplementary Fig. 15). The transport rates of the alkali metal ions were in the range from 1 × 10⁻² to 1 × 10⁻¹ mol h⁻¹ m⁻² with the order of Li⁺ > Na⁺ > K⁺, which also agreed with Eisenman sequence XI (ref. 38). These results were also consistent with the measured ion-mobility sequence (Li⁺ > Na⁺ > K⁺) obtained from the physically confined GO film (Supplementary Discussion and Supplementary Figs. 11 and 13), as well as the simulated ion-mobility sequence obtained from molecular dynamics simulations (Supplementary Note 9 and Supplementary Figs. 16–18). The ions inside the nanoconfined region may be dehydrated (Supplementary Fig. 19)²⁵, and influences from this dehydrated state, free energy barrier, hydration energy and so on^{39,40} may play an important role. The surface of GO possesses abundant oxygen-containing functional groups, such as carboxyl groups (–COOH) and hydroxyl groups (–OH) (Supplementary Fig. 1b), which could lower the activation energy for the dehydration of the cations²⁵. It has been reported that certain

dehydrated ions inside the nanoconfined region have a higher ion mobility and permeability than fully hydrated ions^{38,41}. Dehydrated ions with a more compact structure and a lighter mass, such as Li⁺, may have a higher ion mobility and therefore a higher conductance through the nanofluidic channels³⁸.

To understand the transport properties of the alkali metal ions in the GO nanofluidic channels, a charged-ion dynamic model was established (Supplementary Note 10), where the GO nanofluidic channel was modelled as a subnanopore with a diameter of 2R. Within the modelled subnanopore (2R < 10 Å), the alkali metal ions were assumed to be dehydrated bare ions as the size of the subnanopore is not large enough to allow the hydrated ions to transport through it³⁷. The surrounding medium in the subnanopore was assumed to be moist air (80% RH), which was the same humidity as in our experimental conditions. It was found that the transport-rate sequence of the dehydrated bare alkali metal ions within the subnanopore was Li⁺ > Na⁺ > K⁺ (Fig. 2d). In addition, simulations were also carried out under conditions of dry air (0% RH) and moist air (100% RH) (with the corresponding parameters shown in Supplementary Table 7), and the results from these simulations were not that different from each other (Supplementary Fig. 20). Within the range of the model parameters investigated, the ions would complete the transport process (Supplementary Fig. 21). The above results may be due to Li⁺ possessing the most compact structure and the lightest mass among the three alkali metal ions, and hence it can move faster than the others within the nanoconfined channels of GO. By contrast, the order of the dissociation constants is K_{LiI} < K_{NaI} < K_{KI} (ref. 42), which means that fewer lithium ions may be dissociated when in contact with water. This further proved that the transport rate of Li⁺ may be the highest among the alkali metal ions (Li⁺, Na⁺ and K⁺). Thus, LiI was selected from all of the other AISs for the Ag electrode system.

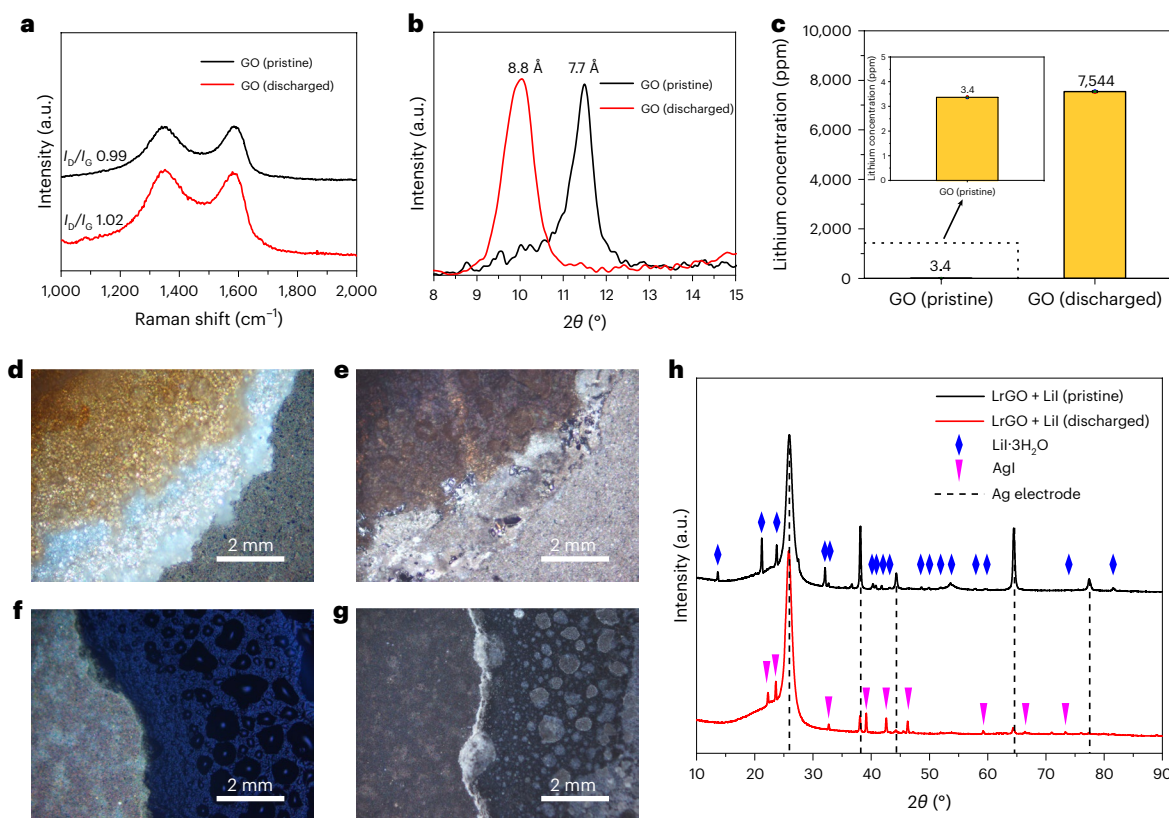


Fig. 3 | Working mechanism of the planar iontronic energy storage device with Lil. **a**, Raman spectra of GO before and after discharge. **b**, X-ray diffraction pattern of GO before and after discharge, which suggests a change in interlayer spacing from 7.7 Å to 8.8 Å. **c**, Elemental lithium concentration in GO before and after discharge, measured using ICP-OES, indicating Li⁺ transportation from LrGO to GO during discharge. Inset: an enlarged view of the pristine GO data. Data are presented as the mean ± s.d., and the error bars represent the s.d. value for three measurements. The coloured blocks (red, blue and green) represent

the corresponding data points. Due to the scale of the figure, the error bars may not be clearly shown. **d, e**, Optical images of the AgNO₃/GO boundary before (**d**) and after (**e**) the device was discharged at 25 °C and 80% RH. **f, g**, Optical images of the Ag electrode/LrGO + Lil boundary before (**f**) and after (**g**) the device was discharged at 25 °C and 80% RH. **h**, X-ray diffraction characterization of the anode side of the device before and after discharge, which suggests the generation of AgI.

For the planar device with Lil, Li⁺ can transport rapidly from the anode (LrGO + Lil) to the cathode side (GO) through the GO/LrGO junction. From the Raman spectrum (Fig. 3a), I_b/I_G for GO after discharge (1.02) is higher than that of pristine GO (0.99). This may be due to the migration of Li⁺ from the anode side to the cathode side, and, similar to K⁺, the insertion of Li⁺ within the GO layers brings more defects. After discharge, the interlayer spacing of GO was increased from 7.7 Å to 8.8 Å, as verified by the X-ray diffraction patterns in Fig. 3b. In addition, ICP-OES indicated that the concentration of elemental lithium in GO increased from 3.4 ppm to 7,544 ppm after discharge, thus providing direct evidence of Li⁺ transportation from LrGO to GO (Fig. 3c). As shown in Fig. 2b and Supplementary Fig. 8, the measured V_{oc} of the planar device with Lil was 1.05 V, which was consistent with the voltage (1.049 V) measured directly using a multimeter (Supplementary Fig. 22). The V_{oc} may come mainly from the dominant E_{redox} with the E_{diff} functioning as a switch to trigger the redox reactions. Furthermore, the discharge plateau and voltage of the planar device with Lil became 0 V as soon as the discharge ended (Supplementary Fig. 23a), indicating that the energy may come mainly from the redox reactions. As indicated above, the redox reactions were designed at the surface of the Ag electrodes, in which AgNO₃ was reduced at the cathode side ($Ag^+ + e^- \rightleftharpoons Ag$) and the Ag electrode was oxidized to form AgI at the anode side ($Ag + I^- \rightleftharpoons AgI + e^-$). Supplementary Figure 23b shows that there is one pair of clear redox peaks, which may be correlated with the reduction of Ag⁺/Ag and the oxidation of Ag/AgI. After multiple

cycles of discharge, AgNO₃ underneath the GO on the Ag electrode (cathode side) changed from a crystalline salt before discharge (Fig. 3d) to metallic Ag particles after discharge (Fig. 3e). Moreover, a crystalline salt was generated on the anode side (Fig. 3f, g) after discharge, which was confirmed to be AgI via energy dispersive spectroscopy and had an Ag/I ratio of about 1:1 (Supplementary Fig. 24). The formation of AgI was further confirmed via X-ray diffraction characterization (Fig. 3h). All of the above results verified the predicted interfacial redox reactions. As the AgI generated on the anode is light-sensitive, the influence of light on the performance of the device was studied, as shown in Supplementary Fig. 25. Although light influenced the energy capacity of the device, it had little effect on the power because of the similar V_{oc} and I_{sc} values in the presence and absence of light. In the future, the device could be encapsulated inside a lightproof packaging material for a more stable output.

To evaluate the rechargeability of the device, galvanostatic charge–discharge experiments at 1 μA were carried out. Unlike commercially available rechargeable batteries, such as Li⁺ batteries⁴³, the voltage of device was rather stable during discharge (Supplementary Fig. 23a), leading to the stable power output ($P = V \times I$) and no waste of energy. As shown in Supplementary Fig. 26, the device could not only be recharged but also exhibited excellent cycling stability. An initial discharge capacity of 2.05 Wh cm⁻³ was obtained. After 400 rechargeable cycles, the discharge capacity still remained as high as 1.99 Wh cm⁻³, and the capacity retention was approximately 97.1%. In addition, the device did not generate any power in the glovebox

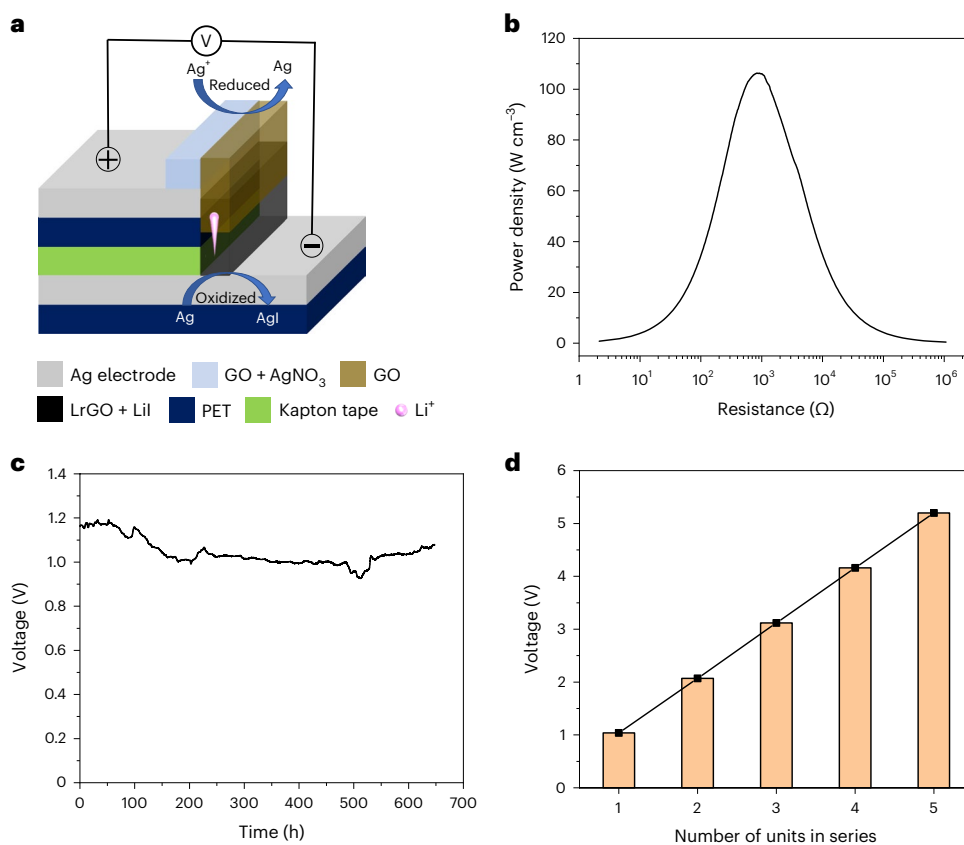


Fig. 4 | Characterization of the vertical iontronic energy storage device. a, Structure of the device. **b**, The volumetric power density as the function of electronic load resistance. **c**, V_{oc} of the device in the ambient environment of Beijing (23.0–23.6 °C, 12.1–20.0% RH). **d**, Plot of the voltage output as a function of the number of device units in series at 25 °C and 80% RH.

(the voltage was zero; Supplementary Fig. 27) where the content of water could be ignored ($H_2O < 0.5$ ppm). Thus, the device could be stored under vacuum or under conditions without any humidity when not being used. This will provide a unique means of overcoming the self-discharge challenge for most batteries and will extend the shelf-life of the device for as long as is required.

Despite the obvious improvement in electric output performance, the planar device with Lil still provided limited power due to the relatively wide electrode gap of 2 mm for ion transport, forming a high internal resistance. By applying the vertical structure design (Fig. 4a), such electrode gap can be reduced to be around 150 μ m. In this case, the electrode gap between the anode and cathode was actually the thickness of the cut insulated polymer film needed to prevent a short circuit. This could exceed the limitation of printing resolution and significantly decrease the internal resistance to increase the I_{sc} of the device. As shown in Supplementary Fig. 28, the current of the device increased with a decrease in the electrode gap, resulting in an improved performance. It has been reported that ions are transported much more rapidly in the horizontal direction than in the vertical direction within the GO film (Supplementary Fig. 29), and that planar confinement in such 2D nanofluidic materials expands the translational degrees of freedom for ionic transport, engendering unusual ion dynamics^{44,45}. The electrode gap of the device, covered by GO, is equal to the thickness of the ion-selective membrane in a conventional osmotic power source. Thus, the vertical structure can effectively decrease the film resistance (internal resistance) and increase the performance of the device. Theoretically, the electrode gap can be decreased to the micrometre level, or even the nanometre level as reported in case of transistor design⁴⁶.

Vertical iontronic device with ultrahigh power

As shown in Fig. 4a, the vertical iontronic energy storage device comprised a PET layer, Ag electrode layers, a Kapton layer, an LrGO + Lil layer, a GO + AgNO₃ layer and a GO film layer. The active area of Li⁺ transport within such a vertical device was 3.4×0.005 mm (Fig. 1c and Supplementary Fig. 30). As the gap between the electrodes was decreased to 150 μ m (Supplementary Fig. 30), the internal resistance was effectively decreased. The device could be discharged at 100 μ A (Fig. 1d), and its I_{sc} was enhanced to almost 1 mA with V_{oc} maintained at around 1.07 V (Fig. 1e). As shown in Fig. 1f, the output power density reached a peak value of 15,900 W m⁻² when the load resistance was approximately 835 Ω (Supplementary Note 1). The vertical iontronic device in this work showed a superior practical performance due to its enhanced power output with a relatively large film area and a shorter ion-transport distance (Supplementary Table 1). In addition, the volumetric energy density and the power density were also calculated to evaluate the practicability of the device. The maximum volumetric specific energy density was calculated to be 9.46 Wh cm⁻³ (Supplementary Fig. 31 and Supplementary Note 1), and the maximum volumetric specific power density was calculated to be 106.33 W cm⁻³ from the electronic load resistance in Fig. 4b (Supplementary Note 1).

To explain the above phenomena, the electrode kinetics of the device were investigated by using the power-law relationship and a.c. electrochemical impedance spectroscopy. The power-law relationship of the current and the scan rate is expressed as $I = av^b$, where I is the peak current, v is the scan rate, a is the intercept and b is the slope calculated from the graph of $\log I$ versus $\log v$. The factor of b , which ranges from 0.5 to 1, aids in distinguishing diffusive and capacitive regulated charge storage behaviour. As discussed in Supplementary Note 11, both the b

value of 0.59 (Supplementary Fig. 32a,b) and the cut-off frequency of 700 Hz (the corresponding relaxation time constant of 1.42 ms) (Supplementary Fig. 32c,d) indicated the pseudocapacitive characteristics of the charge dynamics of the electrodes during the electrochemical process with relatively high ion-transport kinetics. Thus, the device may deliver faster charge transfer and a better power output⁴⁷. It should be noted that the Li⁺ ions were mainly used for charge transfer with an efficient transport capability, while the Ag⁺ ions participated in redox reactions on the surface of the electrodes (Supplementary Fig. 33). The increased power density may be due to the use of 2D nanofluidic materials (GO and LrGO)^{48,49}. Materials with nanostructures may offer a larger fraction of cation storage sites on the surface or in near-surface region⁴⁸ and result in a hybrid energy storage capability to some extent.

In addition, the device possessed a stable V_{oc} of around 1.05 V for more than 600 h in the ambient environment of Beijing (23.0–23.6 °C, 12.1–20.0% RH), as shown in Fig. 4c. The low humidity impeded the ion transport inside the 2D fluidic channels of GO and enabled the V_{oc} to remain stable over a long time period. This also shows the benefits of using GO as a translational transport medium for cations in osmotic energy. To extend the application to power electronics, the output performance of the device connected in series was evaluated. As shown in Fig. 4d, the voltage output of the series-connected units basically increased linearly with the number of units in series, confirming the advantage of the decreased internal resistance in the scaling performance. Two units in series can power an electronic watch (Supplementary Video 1) and an electronic calculator directly (Supplementary Fig. 34a,b and Supplementary Video 2), which were originally powered by a commercial 1.5 V coin cell and a 1.5 V AAA battery, respectively. In addition, four units in series can power an electronic liquid crystal display (LCD) screen directly (Supplementary Fig. 34c–e and Supplementary Video 3).

Conclusions

In summary, we propose a different approach for preparing a solid-state iontronic energy storage device that utilizes osmotic nanoconfined ion-transport properties and interfacial redox reactions, in contrast to the traditional osmotic energy conversion device. Through experiments and simulations, the transport-rate order of alkali metal ions was verified within the GO nanofluidic channels and LiI was selected. The iontronic energy based on osmotic effects could be stored on the edge of a PET substrate and Kapton film. The vertical structure effectively decreased the internal resistance of the device and showed a superior practical performance due to its enhanced power output with a relatively large film area and a shorter ion-transport distance. In addition, because of the volumetric specific energy (9.46 Wh cm⁻³) and power density (106.33 W cm⁻³) obtained, the device could power relatively high energy-consumption electronics, such as LCD screens, directly. Unlike traditional batteries and supercapacitors, the iontronic energy storage device could be printed directly using commercial coating systems or printers in a cost-effective manner. This new approach is proposed to potentially scale up the iontronic energy based on osmotic effects, and further development is still needed to bring it forward in the practical implementation of salinity gradient energy. Overall, the fundamental understanding of nanoconfined ion dynamics and the rational design of iontronic energy systems may pave the way to investigating the influence of other 2D nanomaterials with various nanohierarchical designs and the fine-tuning of redox reactions in the development of futuristic, highly efficient and renewable power sources.

Methods

Materials

GO was prepared from graphite powder (XFNANO) using a modified Hummers method⁵⁰. Graphite powder (1 g), H₃PO₄ (2 ml) and H₂SO₄ (21 ml) were mixed together in an ice bath, and KMnO₄ (3 g) was added slowly. After 2 h, the solution was transferred to a water bath at 35 °C and stirred for 30 min to form a thick paste. Deionized (DI) water (200 ml)

and H₂O₂ (10 ml) were added successively at 95 °C, and the colour of the solution turned from dark brown to bright yellow. After several rounds of centrifugation to wash away soluble salts and any unreacted graphite, the brown-yellow clarified liquid that was collected was the GO dispersion, and this upper liquid portion was freeze-dried to form GO powder. The GO ink was prepared by dispersing the GO powder in DI water. The rGO ink was prepared by adding KOH solution (0.1 mol l⁻¹) to the GO solution (5 mg ml⁻¹) in a ratio of 1:2 (v/v). The LrGO ink was prepared by mixing GO (200 mg), LAA (200 mg), DI water (195 ml) and HCl (5 ml) at 60 °C for 5 h. All of the related chemicals (that is, H₃PO₄, H₂SO₄, KMnO₄, H₂O₂ (30 % w/w), KOH, LAA, HCl (37% w/w), AgNO₃, KI, NaI, LiI, KCl, NaCl, LiCl, acetone (99.5 %), ethanol (99.5 %), [TES][TFSI] and so on) were purchased from Sigma-Aldrich and used as received. The Ag paste was purchased from Chang Sung Corporation. Kapton tape was purchased from 3M Company. DI water with a resistivity of >18 MΩ cm⁻¹ was prepared using a Mili-Q Biocel system. The target material Au (99.9999%) was purchased from ZhongNuo Advanced Material Technology Co., Ltd. The cellulose filter membrane of 0.45 μm pore size was purchased from Sigma-Aldrich.

Fabrication of the iontronic energy storage devices

Commercial PET film (50 μm) was cleaned thoroughly using abundant acetone, ethanol and DI water with a bath sonicator. A computer-controlled commercial CO₂ laser cutter system was used to cut the commercial acrylic plate (2 mm) into pre-designed patterns as the shadow mask, and the shadow mask was then pasted onto the unpatterned PET film with Kapton tape. Au was then deposited onto the exposed PET film with the mask using a magnetron sputtering film deposition system (Denton Discovery 635) to form the Au electrodes. The Ag paste was printed onto the PET film via screen-printing apparatus to form the Ag electrodes, and these were cured in air drying oven at 130 °C for 30 min. An ultrasonic spray-coating system (Cheersonic UAM7000-BN, with a UCA123 spray nozzle) was used to fabricate the iontronic energy storage device (Supplementary Fig. 35). All of the spray-coating experiments were conducted under the same conditions (injection flow rate: 0.05 ml min⁻¹; speed of nozzle movement: 3 mm s⁻¹; height of the nozzle over the fibre: 35 mm; power of the nozzle: 1 W).

Fabrication of the device (Au/GO/rGO/Au). GO ink was sprayed onto and dried on one of the Au electrodes using the ultrasonic spray-coating system to form the GO film, and then rGO ink was sprayed onto and dried on the other Au electrode to form a junction with the GO film.

Fabrication of the devices with AIS. GO/AgNO₃ ink and GO ink were sprayed onto and dried on one of the Ag electrode pads successively to form the cathode side using the ultrasonic spray-coating system, and then the anode Ag electrode side was covered with the LrGO-containing AIS (KI, NaI or LiI) in the same way, overlapping with the GO film to form a junction.

Fabrication of the vertical device. First, the GO/AgNO₃ ink was sprayed onto the Ag electrode pad on the PET substrate. Second, the LrGO/LiI ink was sprayed onto the edge of the Kapton tape. Third, the Ag electrode pad coated with the GO/AgNO₃ layer was cut to form a neat edge, and this was then pasted onto the Kapton tape whose edge was coated with the LrGO + LiI layer. Fourth, the combined edge was coated with GO ink via the same spraying method to form a junction with the LrGO + LiI layer. Last, the other side of the Kapton taps was pasted onto another Ag electrode pad to construct the vertical iontronic energy storage device. The detailed procedures for this are shown in Supplementary Fig. 36 and Supplementary Video 4.

Characterization and measurements

The morphologies of the devices were observed using an SEM (SU8020, Hitachi) with a 5.0 kV accelerating voltage and a 10 μA emission current,

and energy dispersive spectroscopy was used for elemental analysis. A DektakXT stylus profiler (Bruker) was used to profile the morphology of the devices and provide information on the areal values for calculation of the energy and power density. The micro-optical images of the devices were obtained using a metallographic microscope (UMT203i, Chongqing UOP). The temperature, RH and light exposure were controlled using an environmental simulation test chamber (Vötsch Technik). Raman spectra were collected using a LabRAM HR Evolution instrument (Horiba) with a 532 nm laser. Fourier transform infrared spectra were collected using a Bruker VERTEX80v instrument. Zeta potential values were obtained using a Delsamax Pro instrument (Beckman Coulter). The surface charge properties of the GO film were analysed using a SurPASS electrokinetic analyser (Anton Paar) through streaming potential measurements. KCl solution (1 mmol l^{-1}) was used to measure the zeta potential of the GO film under neutral pH. ICP-OES (iCAP 7200 Duo, Thermo Scientific) was used to measure the concentrations of the relevant elements, such as potassium, sodium and lithium, and each sample of GO was measured three times to obtain the standard deviations. All of the samples were tested under the same conditions (pump rate: 29 revolutions per min; nebulizer flow: $0.86 \text{ litres min}^{-1}$; auxiliary gas flow: $0.7 \text{ litres min}^{-1}$; sample flush time: 40 s; radiofrequency power: 1,300 W). X-ray diffraction was carried out using a Bruker D8 ADVANCE system with a Cu K α source. Particle size analysis was measured using BLUEWAVE S3500 laser diffraction analyser (Microtrac) with a 408 nm laser. All electrochemical measurement were carried out using an electrochemical workstation (Multi Autolab M204). The electrochemical impedance spectra were measured over an extended range from 1 MHz to 0.1 Hz.

Data availability

All datasets analysed and generated during the current study are available in both the paper and the Supplementary Information. Source data are provided with this paper.

References

- Esfandiari, A. et al. Size effect in ion transport through ångström-scale slits. *Science* **358**, 511–513 (2017).
- Mitchell, P. Coupling of phosphorylation to electron and hydrogen transfer by a chemi-osmotic type of mechanism. *Nature* **191**, 144–148 (1961).
- Hou, Y. & Hou, X. Bioinspired nanofluidic iontronics. *Science* **373**, 628–629 (2021).
- Jager, E. W. H., Smela, E. & Inganäs, O. Microfabricating conjugated polymer actuators. *Science* **290**, 1540–1545 (2000).
- Bisri, S. Z., Shimizu, S., Nakano, M. & Iwasa, Y. Endeavor of iontronics: from fundamentals to applications of ion-controlled electronics. *Adv. Mater.* **29**, 1607054 (2017).
- Xiao, J. et al. Electrolyte gating in graphene-based supercapacitors and its use for probing nanoconfined charging dynamics. *Nat. Nanotechnol.* **15**, 683–689 (2020).
- Xue, Y. et al. Atomic-scale ion transistor with ultrahigh diffusivity. *Science* **372**, 501–503 (2021).
- Rollings, R. C., Kuan, A. T. & Golovchenko, J. A. Ion selectivity of graphene nanopores. *Nat. Commun.* **7**, 11408 (2016).
- Shao, J.-J., Raidongia, K., Koltonow, A. R. & Huang, J. Self-assembled two-dimensional nanofluidic proton channels with high thermal stability. *Nat. Commun.* **6**, 7602 (2015).
- Yan, C. et al. Engineering 2D nanofluidic Li-ion transport channels for superior electrochemical energy storage. *Adv. Mater.* **29**, 1703909 (2017).
- Siria, A. et al. Giant osmotic energy conversion measured in a single transmembrane boron–nitride nanotube. *Nature* **494**, 455–458 (2013).
- Zhang, Z., Wen, L. & Jiang, L. Nanofluidics for osmotic energy conversion. *Nat. Rev. Mater.* **6**, 622–639 (2021).
- Veeraman, J., Saakes, M., Metz, S. J. & Harmsen, G. Reverse electro dialysis: evaluation of suitable electrode systems. *J. Appl. Electrochem.* **40**, 1461–1474 (2010).
- Zhang, Z. et al. Improved osmotic energy conversion in heterogeneous membrane boosted by three-dimensional hydrogel interface. *Nat. Commun.* **11**, 875 (2020).
- Zhang, Z. et al. Ultrathin and ion-selective Janus membranes for high-performance osmotic energy conversion. *J. Am. Chem. Soc.* **139**, 8905–8914 (2017).
- Zhang, Z. et al. Engineered asymmetric heterogeneous membrane: a concentration-gradient-driven energy harvesting device. *J. Am. Chem. Soc.* **137**, 14765–14772 (2015).
- Xin, W. et al. High-performance silk-based hybrid membranes employed for osmotic energy conversion. *Nat. Commun.* **10**, 3876 (2019).
- Zhou, Y. & Jiang, L. Bioinspired nanoporous membrane for salinity gradient energy harvesting. *Joule* **4**, 2244–2248 (2020).
- Liu, X. et al. Power generation by reverse electro dialysis in a single-layer nanoporous membrane made from core–rim polycyclic aromatic hydrocarbons. *Nat. Nanotechnol.* **15**, 307–312 (2020).
- Feng, J. et al. Single-layer MoS₂ nanopores as nanopower generators. *Nature* **536**, 197–200 (2016).
- Lin, C.-Y. et al. Rectification of concentration polarization in mesopores leads to high conductance ionic diodes and high performance osmotic power. *J. Am. Chem. Soc.* **141**, 3691–3698 (2019).
- Xiao, F. et al. A general strategy to simulate osmotic energy conversion in multi-pore nanofluidic systems. *Mater. Chem. Front.* **2**, 935–941 (2018).
- Jeong, N. et al. Thickness-modulated and interface-engineered MoS₂/TiO₂ heterostructures as a highly active and inexpensive cathode for reverse electro dialysis. *Appl. Surf. Sci.* **504**, 144323 (2020).
- Zhu, X. et al. Integrating reverse-electro dialysis stacks with flow batteries for improved energy recovery from salinity gradients and energy storage. *ChemSusChem* **10**, 797–803 (2017).
- Kim, S. et al. Neuromorphic van der Waals crystals for substantial energy generation. *Nat. Commun.* **12**, 47 (2021).
- Chen, L. et al. Ion sieving in graphene oxide membranes via cationic control of interlayer spacing. *Nature* **550**, 380–383 (2017).
- Koltonow, A. R. & Huang, J. Two-dimensional nanofluidics. *Science* **351**, 1395–1396 (2016).
- Fan, X. et al. Deoxygenation of exfoliated graphite oxide under alkaline conditions: a green route to graphene preparation. *Adv. Mater.* **20**, 4490–4493 (2008).
- Pei, S. & Cheng, H.-M. The reduction of graphene oxide. *Carbon* **50**, 3210–3228 (2012).
- Yang, L. et al. A moisture-enabled fully printable power source inspired by electric eels. *Proc. Natl Acad. Sci. USA* **118**, e2023164118 (2021).
- Raidongia, K. & Huang, J. Nanofluidic ion transport through reconstructed layered materials. *J. Am. Chem. Soc.* **134**, 16528–16531 (2012).
- Wei, D., Yang, F., Jiang, Z. & Wang, Z. Flexible iontronics based on 2D nanofluidic material. *Nat. Commun.* **13**, 4965 (2022).
- Tokuda, H., Md. Abu Bin Hasan Susan, S. T., Hayamizu, K. & Watanabe, M. How ionic are room-temperature ionic liquids? An indicator of the physicochemical properties. *J. Phys. Chem. B* **110**, 19593–19600 (2006).
- Matsumoto, H., Matsuda, T. & Miyazaki, Y. Room temperature molten salts based on trialkylsulfonium cations and bis(trifluoromethylsulfonyl)imide. *Chem. Lett.* **29**, 1430–1431 (2000).

35. Bard, A. J. & Faulkner, L. R. *Electrochemical Methods: Fundamentals and Applications* 2nd edn (Wiley, 2001).
36. Nightingale, E. R. Phenomenological theory of ion solvation. Effective radii of hydrated ions. *J. Phys. Chem.* **63**, 1381–1387 (1959).
37. Daiguji, H. Ion transport in nanofluidic channels. *Chem. Soc. Rev.* **39**, 901–911 (2010).
38. Wen, Q. et al. Highly selective ionic transport through subnanometer pores in polymer films. *Adv. Funct. Mater.* **26**, 5796–5803 (2016).
39. Richards, L. A., Schafer, A. I., Richards, B. S. & Corry, B. The importance of dehydration in determining ion transport in narrow pores. *Small* **8**, 1701–1709 (2012).
40. Yang, L. & Garde, S. Modeling the selective partitioning of cations into negatively charged nanopores in water. *J. Chem. Phys.* **126**, 084706 (2007).
41. Razmjou, A. et al. Design principles of ion selective nanostructured membranes for the extraction of lithium ions. *Nat. Commun.* **10**, 5793 (2019).
42. Bruckenstein, S. & Mukherjee, L. M. Equilibria in ethylenediamine. I. The relative dissociation constants of silver salts and alkali metal halides. *J. Phys. Chem.* **64**, 1601–1607 (1960).
43. Lu, L.-L. et al. Extremely fast-charging lithium ion battery enabled by dual-gradient structure design. *Sci. Adv.* **8**, eabm6624 (2022).
44. Chmiola, J. et al. Anomalous increase in carbon capacitance at pore sizes less than 1 nanometer. *Science* **313**, 1760–1763 (2006).
45. Futamura, R. et al. Partial breaking of the Coulombic ordering of ionic liquids confined in carbon nanopores. *Nat. Mater.* **16**, 1225–1232 (2017).
46. Wu, F. et al. Vertical MoS₂ transistors with sub-1-nm gate lengths. *Nature* **603**, 259–264 (2022).
47. Sankar, K. V. & Selvan, R. K. The preparation of MnFe₂O₄ decorated flexible graphene wrapped with PANI and its electrochemical performances for hybrid supercapacitors. *RSC Adv.* **4**, 17555–17566 (2014).
48. Simon, P., Gogotsi, Y. & Dunn, B. Where do batteries end and supercapacitors begin? *Science* **343**, 1210–1211 (2014).
49. Aricò, A. S. et al. Nanostructured materials for advanced energy conversion and storage devices. *Nat. Mater.* **4**, 366–377 (2005).
50. Talyzin, A. V. et al. Brodie vs Hummers graphite oxides for preparation of multi-layered materials. *Carbon* **115**, 430–440 (2017).

Acknowledgements

We thank X. Xie from the group of D.W. at Beijing Institute of Nanoenergy and Nanosystems for their help with the computational studies. This work was supported by the Beijing Natural Science Foundation (grant number IS23040), the National Natural Science Foundation (grant number 62274101) and the Research Grants Council of the Hong Kong Special Administrative Region (grant numbers C6020-22G and C7001-22Y).

Author contributions

D.W. and Z.L.W. proposed the idea and supervised the whole project. D.W., F.Y. and P.P. designed the experiment and performed the device fabrication and characterization. F.Y. and P.P. synthesized the samples. F.Y., P.P., X.L. and S.L. performed the corresponding measurements. Z.-Y.Y., H.F., H.L., T.-L.R. and Y.Z. performed the computational studies. D.W. and F.Y. wrote the paper. All the authors discussed the results and commented on the paper.

Competing interests

The authors declare no competing interests.

Additional information

Supplementary information The online version contains supplementary material available at <https://doi.org/10.1038/s41560-023-01431-4>.

Correspondence and requests for materials should be addressed to Zhong Lin Wang or Di Wei.

Peer review information *Nature Energy* thanks the anonymous reviewers for their contribution to the peer review of this work.

Reprints and permissions information is available at www.nature.com/reprints.

Publisher's note Springer Nature remains neutral with regard to jurisdictional claims in published maps and institutional affiliations.

Springer Nature or its licensor (e.g. a society or other partner) holds exclusive rights to this article under a publishing agreement with the author(s) or other rightsholder(s); author self-archiving of the accepted manuscript version of this article is solely governed by the terms of such publishing agreement and applicable law.

© The Author(s), under exclusive licence to Springer Nature Limited 2024